Chinese Journal of Structural Chemistry

ARTICLE

Asymmetric Structure Awakened n-π* Electron Transition in Sulfur and Selenium Co-doped g-C_3N_4 with Efficient Photocatalytic Performance

Tian Liu[1], Yunfeng Li[1]*, Hejia Sun[2], Min Zhang[1], Zhiling Xia[1] and Qing Yang[1]

[1]*College of Environmental and Chemical Engineering, Xi'an Key Laboratory of Textile Chemical Engineering Auxiliaries, Xi'an Polytechnic University, Xi'an 710000, China*

[2]*College of Physical Education, Xi'an Polytechnic University, Xi'an 710000, China*

ABSTRACT Sulfur and selenium co-doped graphitic carbon nitride (SSCN) with efficient photocatalytic activity was synthesized by synchronously introducing sulfur and selenium atoms into the melon structure of g-C_3N_4 (GCN) via a facile solid-phase thermal reaction of GCN and SeS_2. The as-prepared SSCN possesses a larger specific surface area with a richer pore structure that provides more active centers for catalytic reaction. More importantly, the asymmetric structure of SSCN due to introducing sulfur and selenium not only maintains an easier activation of π-π* electron transition but also awakens the n-π* electron transition in g-C_3N_4. Moreover, the n-π* electron transition of SSCN can be controlled through changing the amount of SeS_2, which can greatly extend the photo-response range to 600 nm. As a result, the SSCN samples show an excellent photo-degradation performance for typical antibiotic of tetracycline hydrochloride (TC). The specific degradation route and main intermediates of TC based on liquid chromatograph mass spectrometer (LC-MS) analysis are also investigated and discussed.

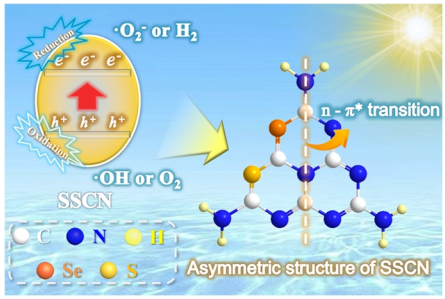

Keywords: photocatalysis, Co-doping, n-π* transition, charges transfer, photo-degradation

n INTRODUCTION

The improvement of human living standard is inseparable from the development of modern industry followed by a large number of organic pollutants.[1,2] The pollutants are difficult to degrade and easy to diffuse, which has become a common challenge faced by all mankind.[3,4] The traditional methods for removing organic pollutants, including physical adsorption, chemical treatment and biological decomposition, have many disadvantages, such as high cost, harmful by-products and complex process.[5-10] Therefore, the semiconductor photocatalytic technology has attracted increasing attention for its potential in wastewater treatment due to its green and energy saving characteristics.[11-17] So far, many photocatalysts have been developed, such as TiO_2 and its nanocomposites.[18,19] TiO_2 is a kind of widely used commercial photocatalyst, but it can only absorb ultraviolet light and has no visible light response.[20-24] Therefore, photocatalysts with visible light response have become an important research topic in recent years, including ZnO,[25] SnO_2,[26] CdS,[27] $BiVO_4$,[28] Ta_3N_5,[29,30] g-C_3N_4[31-33] and so on. Among them, g-C_3N_4 as a non-metallic organic semiconductor material has become an extremely attractive visible light photocatalyst due to its suitable band structure (2.7 eV), high chemical stability, and low production cost.[34-36] However, the original g-C_3N_4 has some inherent disadvantages, such as small specific surface area, poor visible light utilization and high carrier recombination rate.[37-39]

In order to overcome the above drawbacks, researchers have developed many strategies to improve the photocatalytic performance of g-C_3N_4, such as metal and non-metal doping,[40-43] introduction of vacancy defects,[44] morphology modulation,[45,46] construction of heterojunctions,[47-49] etc. Among these methods, non-metallic doping is an attractive strategy to adjust the composition and morphology of g-C_3N_4-based photocatalysts, which can maintain the non-metallic properties of g-C_3N_4 with low cost, earth-abundant as well as stable and adjustable properties. By doping non-metallic elements, the band structure of g-C_3N_4 can be adjusted to tune its light-absorption ability and redox capacity, and the photocatalytic activity can be improved.[50] Lv et al.[51] prepared S-doped g-C_3N_4 nanosheets using thiourea as precursor system, and the obtained S-doped g-C_3N_4 nanosheets have a high specific surface area with a reduced bandgap and increased surface N defects. Kumar et al.[52] synthesized a novel in-situ Se-doped g-C_3N_4 nanosheet by a simple one-pot two-step strategy. The Se doping generated an intermediate state in g-C_3N_4, which could significantly extend the light absorption to 570 nm. Thus, the Se-doped g-C_3N_4 nanosheet showed an enhanced efficiency for solar fuel production from CO_2. Although most previous reports have focused on single-element doping, some studies have shown that co-doping with more than one nonmetallic atom is more efficient than single-element doping. For example, (P, S) co-doping,[53] (S, O) co-doping[54] and (C, I) co-doping[55] all show a higher photocatalytic activity and unusual physicochemical characteristic. Therefore, it is necessary to study the multi-element doping in g-C_3N_4 framework and explore the mechanism of its enhanced photocatalytic activity.[56]

In this work, sulfur and selenium co-doped graphitic carbon nitride (SSCN) with efficient photocatalytic activity was synthesized by synchronously introducing sulfur and selenium atoms into the

DOI: 10.14102/j.cnki.0254-5861.2022-0152

melon structure of g-C_3N_4 (GCN) via a facile solid-phase thermal reaction of GCN and SeS_2. The as-prepared SSCN possesses a larger specific surface area with a richer pore structure that provides more active centers for catalytic reaction. More importantly, the asymmetric structure of SSCN due to introducing sulfur and selenium not only maintains the easier activation of π-π* electron transition but also awakens the n-π* electron transition in g-C_3N_4. Moreover, the n-π* electron transition of SSCN can be controlled through changing the amount of SeS_2, which can greatly extend the photo-response range to 600 nm. As a result, the SSCN samples show an excellent photo-degradation performance for typical antibiotic of tetracycline hydrochloride (TC).

n RESULTS AND DISCUSSION

Structure and Property Analysis. Figure 1a displays the XRD patterns of the synthesized samples. Two distinct diffraction peaks of all the samples locate at ~13.2° and 27.5°, corresponding to the (1 0 0) and (0 0 2) planes of g-C_3N_4, respectively. Compared with GCN, SSCN samples display a lower intensity and broader half peak of the (0 0 2) crystal plane, which is ascribed to the fact that the S and Se doping affects the periodic structure of g-C_3N_4. This decreased periodic structure not only maintains the easier activation of π-π* electron transition, but also awakens the n-π* electron transition in g-C_3N_4. The chemical structures of the GCN and SSCN samples were further investigated by the FT-IR spectrum (Figure 1b). The characteristic vibration peaks of as-prepared photocatalysts at 810, 1200~1600 and 3000~3500 cm^{-1} are attributed to the characteristics from tri-s-triazine ring units, stretching modes of aromatic C-N heterocycle, and stretching vibration of amine groups (NHx), respectively. No obvious C-S and C-Se peaks could be observed, mainly due to the low content of SeS_2 and another factor which may be that the characteristic peaks of C-S and C-Se are overlapped with the stretching vibration mode of g-C_3N_4.

The surface compositions and chemical states of SSCN-50 sample are examined by XPS characterization. Figure 2a shows the C 1s spectrum with three characteristic peaks at about 284.8, 286.9 and 288.4 eV corresponding to C-C, C-NH_X and N-C=N, respectively. It is worth noting that two new peaks appear at 282.8 and 283.6 eV, attributed to C-Se and C-S, respectively. As shown in Figure 2b, the N 1s spectrum of SSCN-50 displays three peaks at 396.9, 398.7 and 401.1 eV, which can be respectively associated with N_2C, N_3C and N-Hx. The peak of S element in Figure 2c can be divided into 157.0, 159.4, 161.9 and 164.5 eV assigned to

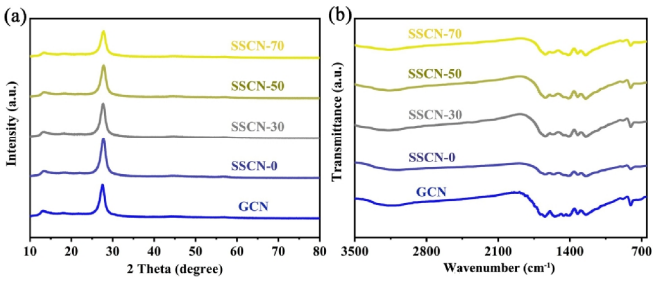

Figure 1. (a) XRD patterns and (b) FT-IR spectra of the as-prepared samples.

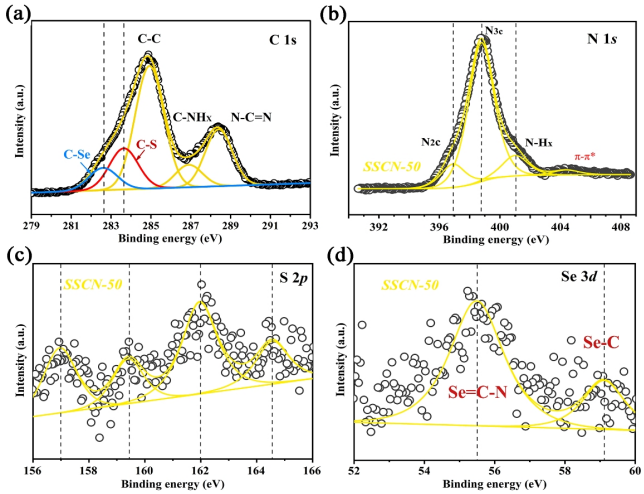

Figure 2. The high-resolution XPS spectra of C 1s (a), N 1s (b), S 2p (c) and Se 3d (d) for SSCN-50 sample.

S 2p in SSCN-50. The Se 3d spectrum is deconvoluted into two main peaks with binding energies of 55.5 and 59.1 eV, corresponding to Se=C-N and C-Se (Figure 2d), respectively.[57,58] The above results indicate that the sulfur and selenium co-doped g-C_3N_4 has been synthesized.

The morphologies and microstructures of GCN, SSCN-0 and SSCN-50 photocatalysts are characterized by SEM and TEM. As shown in Figure 3a-c, the SEM images of GCN, SSCN-0 and SSCN-50 photocatalysts show the 2D structure characteristic. However, compared with GCN and SSCN-0, the surface of SSCN-50 becomes slightly rough due to the doping of S and Se in g-C_3N_4. As shown in Figure 3d-g, the EDX element mapping images display that the C, N, S and Se are homogeneously distributed in the SSCN-50 sample. The TEM images of GCN, SSCN-0 and SSCN-50 samples are shown in Figure 3h-j, and some appeared pores increase the specific surface area of SSCN-50, which is consistent with the N_2 adsorption-desorption result. In

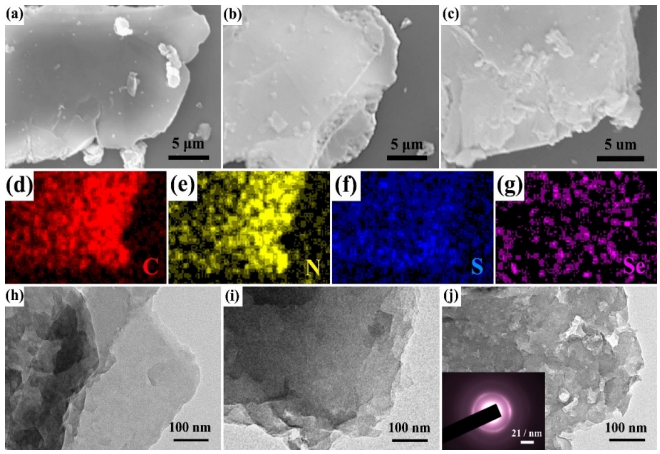

Figure 3. SEM images of (a) GCN, (b) SSCN-0 and (C) SSCN-50 samples. Elemental mapping images of (d) C, (e) N, (f) S and (g) Se for SSCN-50 sample. TEM images of (h) GCN, (i) SSCN-0, (j) SSCN-50 and SAED image of SSCN-50 (inset of j).

Chin. J. Struct. Chem. **2022**, 41, 2206055-2206061
DOI: 10.14102/j.cnki.0254-5861.2022-0152

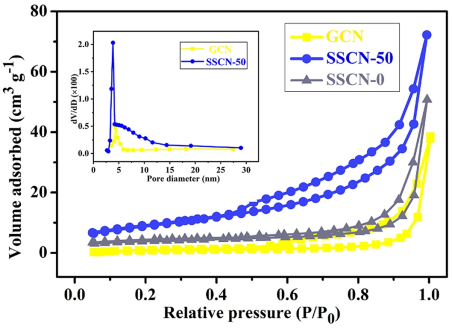

Figure 4. N_2 adsorption-desorption isotherms and corresponding pore size distribution curves of GCN and SSCN-50 samples.

addition, the two diffraction rings in SAED pattern (inset of Figure 3j) correspond to the (1 0 0) and (0 0 2) planes of SSCN-50.

The N_2 adsorption-desorption isotherms and pore size distribution curves of GCN and SSCN-50 are shown in Figure 4. It is noted that the samples show a similar type-IV adsorption-desorption isotherms and H_3 hysteresis loop, implying the presence of mesopore in photocatalysts. Notably, the specific surface area of SSCN-50 is about 32.43 $m^2 g^{-1}$, which is almost 4 times higher than that of GCN (8.06 $m^2 g^{-1}$). Moreover, the specific surface area of SSCN-0 has been also tested to be 8.67 $m^2 g^{-1}$. The increased surface area is attributed to the rich pore structure (inset of Figure 4) resulting from S and Se co-doping. It is well known that the large specific surface area with more active sites is beneficial for improving the photocatalytic performance.

The light absorption and utilization of the prepared samples are characterized by UV-vis DRS. As shown in Figure 5a, the SSCN samples show an enhanced light absorption in both UV and visible light regions. A typical absorption edge around 390 nm is identified as the intrinsic electronic transition (π-π*) of g-C_3N_4. Notably, a new absorption peak at about 490 nm appears in the UV-vis DRS of SSCN samples, which is ascribed to the (n-π*) electronic transition.[59] The generation of (n-π*) electronic transition can be

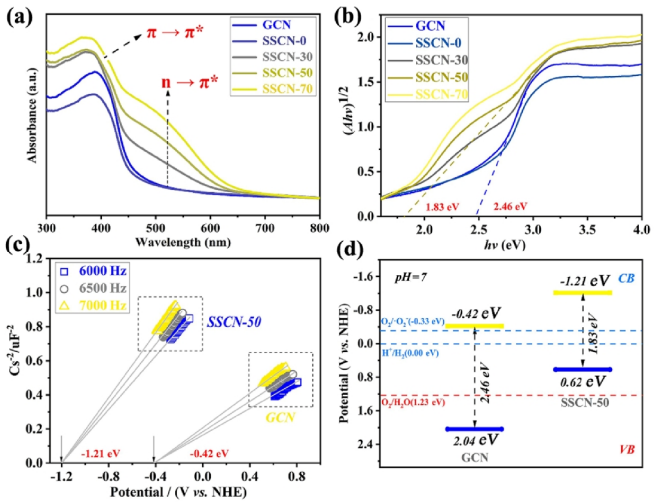

Figure 5. (a) UV-vis DRS spectra and (b) Kubelka-Munk plots of the as-prepared samples. (c) Mott-Schottky plot and (d) band structure of GCN and SSCN-50 samples.

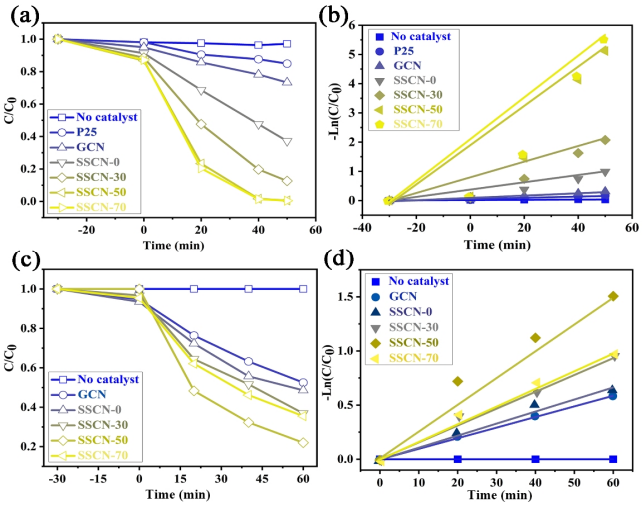

Figure 6. (a) Photocatalytic degradation of RhB and (b) the corresponding degradation kinetics for the as-prepared samples. (c) Photocatalytic degradation of TC and (d) the corresponding degradation kinetics for the as-prepared samples.

attributed to the asymmetrical structure of SSCN samples resulting from S and Se co-doping. According to the Kubelka-Munk function $(F(R)h\nu)^n$ versus the energy of exciting light ($h\nu$), the bandgap of GCN and SSCN-50 is calculated to be 2.46 and 1.83 eV, respectively (Figure 5b). The Mott-Schottky curves are applied to determine the conduction band (CB) potential of GCN and SSCN-50 samples. As shown in Figure 5c, the GCN and SSCN-50 samples exhibit typical n-type semiconductor characteristics. The CB potentials of GCN and SSCN-50 are determined to be -0.42 and -1.21 V (*vs.* NHE), respectively. Through combining the value of bandgap and CB potential, the valence band (VB) potentials of GCN and SSCN-50 are determined to be 2.04 and 0.62 V, respectively. The band structure of as-prepared samples is shown in Figure 5d.

Photocatalytic Activity. The photocatalytic activity of prepared samples was analyzed by degrading antibiotic of TC and typical dye of RhB under visible light irradiation. As depicted in Figure 6a, no significant degradation of RhB is observed without the addition of any photocatalyst. For P25 and GCN samples, only 15.1% and 26.7% of RhB can be respectively removed after 45 minutes of illumination. The photocatalytic activities of all SSCN samples are greatly improved and the highest efficiency of RhB degradation of SSCN-50 can attain 99.4%. The kinetic profile of RhB can be approximated by linearly transforming $\ln(C_0/C_t) = kt$ to a quasi-level process shown in Figure 6b. The result shows that the degradation rate constant for SSCN-50 (0.067 min^{-1}) is about 16.8 times that of GCN (0.004 min^{-1}). In addition, the antibiotic of TC is also used to evaluate the photocatalytic performance in this work. The SSCN-50 sample also exhibits the highest photocatalytic activity (Figure 6c). Especially, 78% of TC could be degraded after 60 min light irradiation. As shown in Figure 6d, the kinetic curve of TC can be approximated as a pseudo first-order process by linear transformation $\ln(C_0/C_t) = kt$, indicating the degradation rate of SSCN-50 (0.025 min^{-1}) to be about 2.5 times that of GCN (0.010 min^{-1}).

DOI: 10.14102/j.cnki.0254-5861.2022-0152

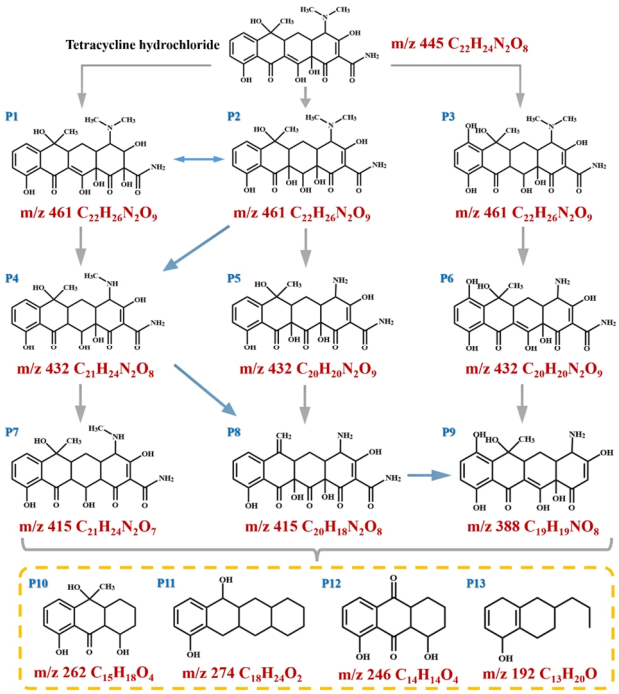

Figure 7. Specific degradation pathways of TC based on the main intermediates in degradation process.

The above results show that the photocatalytic activity of g-C_3N_4 could be significantly improved by S and Se co-doping.

The specific degradation route for TC based on major intermediates is also proposed by LC-MS characterization. As shown in Figure 7, the intermediates P1 (m/z 461), P2 (m/z 461) and P3 (m/z 461) originate from TC cleavage by double bond breakage and hydroxyl addition. The intermediates P1 and P2 are further degraded by the loss of N-methyl and hydroxyl groups to generate intermediate P4 (m/z 432), which is then degraded by removing hydroxyl groups to produce intermediate P7 (m/z 415). The intermediate P5 (m/z 432) is produced by removing N-methyl and hydroxyl groups from P2 to produce both amino and carbonyl groups, and then P5 is further degraded by losing hydroxyl and methyl groups to produce methylene groups to form the intermediate P8 (m/z 415). The intermediate P6 is generated from P3 by removing n-methyl and producing amino group at the same time. In addition, the intermediate P9 (m/z 388) is produced through a multi-step degradation process of intermediates P6 and P8. The obtained P7, P8 and P9 are further converted to low molecular weight organic compounds (P10-P13) and eventually degraded to CO_2 and H_2O.

Possible Photocatalytic Mechanism. The PL spectra are carried out to investigate the separation and migration of photo-generated carriers.[60-63] As shown in Figure 8a, the SSCN-50 sample shows an evident quenching of PL intensity compared with GCN, revealing that the recombination rate of photo-induced electrons and holes for SSCN-50 is effectively suppressed. Meanwhile, the time-resolved PL spectra of GCN, SSCN-0 and SSCN-50 are recorded (Figure 8b). The photoluminescence intensity of SSCN-50 decays is much faster than that of GCN. The emission

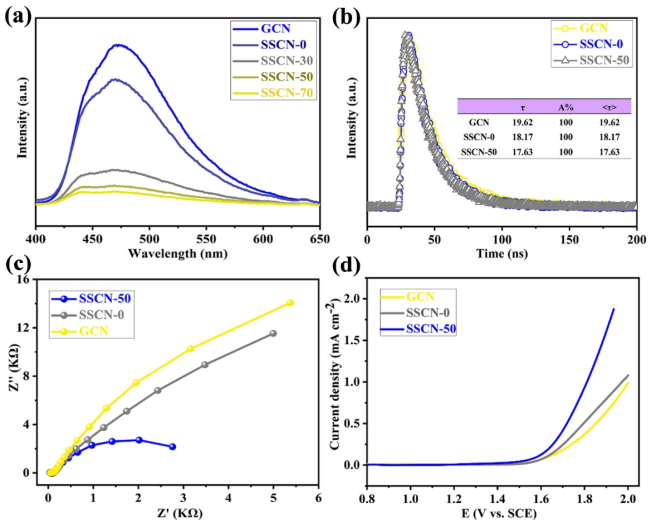

Figure 8. (a) Steady-state PL spectra of the as-prepared samples. (b) Time-resolved PL spectra, (c) EIS tests and (d) LSV curves of GCN, SSCN-0 and SSCN-50 samples.

decay data could be fitted by double-exponential formula with one component of life time. It is found that the photo-generated carrier lifetime of SSCN-50 (17.63 ns) is less than that of GCN (19.62 ns) due to the fact that the introduction of selenium and sulfur can shorten the migration path of photo-generated electrons and promote the electron transfer of g-C_3N_4.[64-66] As shown in Figure 8c, by comparison with the GCN and SSCN-0, SSCN-50 shows a significantly decreased arc radius, suggesting a low charge transfer resistance. The LSV curves of the samples show that the over potential of SSCN-50 sample is significantly reduced compared to GCN and SSCN-0 during the whole voltage range (Figure 8d), thus demonstrating a fast charge transfer and separation in SSCN-50.

n CONCLUSIONS

In summary, sulfur and selenium co-doped graphitic carbon nitride (SSCN) has been synthesized successfully by synchronously introducing sulfur and selenium atoms into the melon structure of g-C_3N_4. The as-prepared SSCN possesses a larger specific surface area with a richer pore structure that provides more active centers for catalytic reaction. More importantly, the asymmetric structure of SSCN due to introducing sulfur and selenium not only maintains the easier activation of π-π* electron transition but also awakens the n-π* electron transition in g-C_3N_4. The experimental results indicate that SSCN-50 shows the best photocatalytic performance, achieving 78.0% and 99.4% degradation of antibiotics (TC) and organic dyes (RhB), which is 2.5 and 16.8 times higher than GCN, respectively. This work demonstrates a simple, low-cost and sustainable strategy for the preparation of high-performance non-metallic g-C_3N_4 photocatalyst.

n EXPERIMENTAL

Preparation of Sulfur and Selenium Co-doped g-C_3N_4 (SSCN). All chemicals in this experiment were analytical grade and used without further purification. The sulfur and selenium co-doped g-

DOI: 10.14102/j.cnki.0254-5861.2022-0152

C_3N_4 was fabricated via a facile solid-state thermal treatment of g-C_3N_4 and SeS_2. In a typical synthesis, 5 g of melamine was added into an alumina crucible with a cover and then heated at 550 ℃ for 2 h by using a ramp rate of 5 ℃ min^{-1}. The sample was fabricated and grounded into powder. Afterwards, 300 mg of g-C_3N_4 was mixed with a certain amount of SeS_2 evenly, and then put into an alumina crucible with a cover. Subsequently, the mixture was heated at 400 ℃ for 1 h at a heating rate of 5 ℃ min^{-1}. The as-prepared samples were labeled as SSCN-0, SSCN-30, SSCN-50 and SSCN-70, when the mass of SeS_2 in the mixture is 0, 30, 50 and 70 mg, respectively. The pure g-C_3N_4 (GCN) was prepared by direct calcination of melamine at 550 ℃ for 2 h.

Characterization. X-ray diffraction (XRD) pattern of the photocatalyst was analyzed by a Dmax Rapid II diffractometer. Fourier transform infrared spectroscopy (FT-IR) was measured by a Spotlight 400 spectrometer. X-ray photoelectron spectroscopy (XPS) was examined by a Thermo ESCALAB 250 XPS equipment with standard monochromatic light source. Scanning electron microscopy (SEM) image and energy dispersive X-ray (EDX) elemental mapping were tested by a FEI Quanta 450 FEG microscope. Electrochemical impedance spectroscopy (EIS), Mott-Schottky plot and linear sweep voltammetry (LSV) were conducted by using a standard three-electrode cell with probe solution as the electrolyte, platinum as a counter, saturated calomel electrode as a reference electrode and ITO glass deposited with sample as a working electrode. Photoluminescence (PL) spectrum was determined by a FLSP920 Edinburgh Fluorescence Spectrometer. UV-vis diffuse reflectance spectrum (UV-vis DRS) was performed on a Cary 500 spectrometer.

Photocatalytic Test. To evaluate the photocatalytic efficiency of as-prepared samples, 30 mg photocatalysts for the degradation of typical antibiotic TC (30 mg/L, 80 mL) and 60 mg photocatalysts for degradation of RhB (10 mg/L, 80 mL) were studied by using 500 W Xe lamp as light source (λ > 420 nm). To ensure the adsorption-desorption equilibrium between the target contaminants and photocatalysts, the suspension was treated by ultrasonic for 5 min and stirred in the dark for 30 min. During the irradiation process, 3 mL suspension was extracted at given time intervals, then centrifuged at 10000 rpm for 5 min to remove the solid photocatalysts. The residual concentration of antibiotic TC and RhB was analyzed by a UV-vis-NIR spectrophotometer.

n ACKNOWLEDGEMENTS

This work is supported by the National Natural Science Foundation of China (22008185), Shaanxi Provincial Key Research and Development Program (2022GY-166), and Scientific Research Program Funded by Shaanxi Provincial Education Department (19JK0376).

n AUTHOR INFORMATION

Corresponding author. Email: liyf377@nenu.edu.cn

n COMPETING INTERESTS

The authors declare no competing interests.

n ADDITIONAL INFORMATION

Supplementary information is available for this paper at http://manu30.magtech.com.cn/jghx/EN/10.14102/j.cnki.0254-5861.2022-0152

For submission: https://mc03.manuscriptcentral.com/cjsc

n REFERENCES

(1) Liu, Q.; Li, Z.; Li, J.; Zhan, F.; Zhai, D.; Sun, Q.; Xiao, Z.; Luo, H.; Zhang, D. Three dimensional $BaTiO_3$ piezoelectric ceramics coated with TiO_2 nanoarray for high performance of piezo-photoelectric catalysis. *Nano Energy* **2022**, 98, 107267.

(2) Huang, J.; Li, C.; Hu, X.; Fan, J.; Zhao, B.; Liu, E. K_2HPO_4-mediated photocatalytic H_2 production over NiCoP/RP heterojunction. *Chin. J. Struct. Chem*. **2022**, 41, 2022062-2022068.

(3) Li, S.; Wang, C.; Cai, M.; Yang, F.; Liu, Y.; Chen, J.; Zhang, P.; Li, X.; Chen, X. Facile fabrication of TaON/Bi_2MoO_6 core-shell S-scheme heterojunction nanofibers for boosting visible-light catalytic levofloxacin degradation and Cr (VI) reduction. *Chem. Eng. J.* **2022**, 428, 131158.

(4) Li, Z.; Huang, D.; Zhou, C.; Xue, W.; Lei, L.; Deng, R.; Yang, Y.; Chen, S.; Wang, W.; Wang, Z. Metal-free carbon nitride with boosting photo-redox ability realized by the controlled carbon dopants. *Chem. Eng. J.* **2020**, 382, 122657.

(5) Bie, C.; Yu, H.; Cheng, B.; Ho, W.; Fan, J.; Yu, J. Design, fabrication, and mechanism of nitrogen-doped graphene-based photocatalyst. *Adv. Mater.* **2021**, 33, 2003521.

(6) Wang, Z.; Hong, J.; Ng, S.; Liu, W.; Huang, J.; Chen, P.; Ong, W. Recent progress of perovskite oxide in emerging photocatalysis landscape: water splitting, CO_2 reduction, and N_2 fixation. *Acta Phys. -Chim. Sin.* **2021**, 37, 2011033.

(7) Cheng, C.; He, B.; Fan, J.; Cheng, B.; Cao, S.; Yu, J. An inorganic/organic S-scheme heterojunction H_2 production photocatalyst and its charge transfer mechanism. *Adv. Mater.* **2021**, 33, 2100317.

(8) Candish, L.; Collins, K.; Cook, G.; Douglas, J.; Suarez, A.; Jolit, A.; Keess, S. Photocatalysis in the life science industry. *Chem. Rev.* **2022**, 122, 2907-2980.

(9) Wang, H.; Lin, X.; Zhao, X.; Li, C.; Song, X.; Zhang, P.; Huo, P.; Li, X. A review on heterogeneous photocatalysis for environmental remediation: from semiconductors to modification strategies. *Chin. J. Catal.* **2022**, 43, 178-214.

(10) Ling, Z.; Ng, S.; Ong, W. Tailor-engineered 2D cocatalysts: harnessing electron-hole redox center of 2D g-C_3N_4 photocatalysts toward solar-to-chemical conversion and environmental purification. *Adv. Funct. Mater.* **2022**, 2111875.

(11) Jiang, Z.; Chen, Q.; Zheng, Q.; Shen, R.; Zhang, P.; Li, X. Constructing 1D/2D Schottky-based heterojunctions between $Mn_{0.2}Cd_{0.8}S$ nanorods and Ti_3C_2 nanosheets for boosted photocatalytic H_2 evolution. *Acta Phys. -Chim. Sin.* **2021**, 37, 2010059.

(12) He, Y.; Li, J.; Sun, M.; Yuan, C.; Chen, R.; Sheng, J.; Leng, G.; Dong, F. Bi quantum dots implanted 2D C-doped BiOCl nanosheets: enhanced visible light photocatalysis efficiency and reaction pathway. *Chin. J. Catal.* **2020**, 41, 1430-1438.

(13) Li, S.; Wang, C.; Liu, Y.; Cai, M.; Wang, Y.; Zhang, H.; Guo, Y.; Zhao, W.; Wang, Z.; Chen, X. Photocatalytic degradation of tetracycline antibiotic by a novel $Bi_2Sn_2O_7$/Bi_2MoO_6 S-scheme heterojunction: performance, mechanism insight and toxicity assessment. *Chem. Eng. J.* **2022**, 429, 132519.

(14) Zhang, Y.; Qiu, J.; Zhu, B.; Fedin, M.; Cheng, B.; Yu, J.; Zhang, L.

DOI: 10.14102/j.cnki.0254-5861.2022-0152

ZnO/COF S-scheme heterojunction for improved photocatalytic H_2O_2 production performance. *Chem. Eng. J.* **2022**, 444, 136584.

(15) Zhang, M.; Li, Y.; Chang, W.; Zhu, W.; Zhang, L.; Jin, R.; Xing, Y. Negative inductive effect enhances charge transfer driving in sulfonic acid functionalized graphitic carbon nitride with efficient visible-light photocatalytic performance. *Chin. J. Catal.* **2022**, 43, 526-535.

(16) Yu, J.; Zhang, T.; Wu, N. Solar photocatalysis. *Sol. RRL* **2021**, 5, 2100037.

(17) Wang, Y.; Zhu, B.; Cheng, B.; Macyk, W.; Kuang, P.; Yu, J. Hollow carbon sphere-supported Pt/CoO_x hybrid with excellent hydrogen evolution activity and stability in acidic environment. *Appl. Catal. B* **2022**, 314, 121503.

(18) Oh, S.; Kim, J.; Hwang, H.; Kim, D.; Kim, J.; Park, G.; Kim, J.; Lee, Y.; Lee, H. Band restructuring of ordered/disordered blue TiO_2 for visible light photocatalysis. *J. Mater. Chem. A* **2021**, 9, 4822.

(19) Sayed, M.; Yu, J.; Liu, G.; Jaroniec, M. Non-noble plasmonic metal-based photocatalysts. *Chem. Rev.* **2022**, 122, 10484-10537.

(20) Zhou, J.; Li, X.; Ma, X.; Sheng, W.; Lang, X. Cooperative photocatalysis of dye-TiO_2 nanotubes with $TEMPO^+$ BF_4^- for selective aerobic oxidation of amines driven by green light. *Appl. Catal. B* **2021**, 296, 120368.

(21) Wu, S.; Li. X.; Tian, Y.; Lin, Y.; Hu, Y. Excellent photocatalytic degradation of tetracycline over black anatase-TiO_2 under visible light. *Chem. Eng. J.* **2021**, 406, 126747.

(22) Sheng, W.; Shi, J.; Hao, H.; Li, X.; Lang, X. Polyimide-TiO_2 hybrid photocatalysis: visible light-promoted selective aerobic oxidation of amines. *Chem. Eng. J.* **2020**, 379, 122399.

(23) Xu, C.; Lv, P. Photo-assisted deposited titanium dioxide film and the enhancement of its photocatalytic water splitting activity. *Chin. J. Struct. Chem.* **2021**, 40, 1223-1230.

(24) Wang, L.; Cheng, B.; Zhang, L.; Yu, J. In situ irradiated XPS investigation on S-scheme TiO_2@$ZnIn_2S_4$ photocatalyst for efficient photocatalytic CO_2 reduction. *Small* **2021**, 17, 2103447.

(25) Wan, Y.; Li, J.; Ni, J.; Wang, C.; Ni, C.; Chen, H. Crystal-facet and microstructure engineering in ZnO for photocatalytic NO oxidation. *J. Hazard. Mater.* **2022**, 435, 129073.

(26) Sun, Y.; Zhu, Q.; Bai, B.; Li, Y.; He, C. Novel all-solid-state Z-scheme SnO_2/Pt/In_2O_3 photocatalyst with boosted photocatalytic performance on water splitting and 2,4-dichlorophenol degradation under visible light. *Chem. Eng. J.* **2020**, 390, 124518.

(27) Xu, J.; Zhong, W.; Gao, D.; Wang, X.; Wang, P.; Yu, H. Phosphorus-enriched platinum diphosphide nanodots as a highly efficient cocatalyst for photocatalytic H_2 evolution of CdS. *Chem. Eng. J.* **2022**, 439, 135758.

(28) Zhang, Q.; Liu, M.; Zhou, W.; Zhang, Y.; Hao, W.; Kuang, Y.; Liu, H.; Wang D.; Liu L.; Ye, J. A novel Cl-modification approach to develop highly efficient photocatalytic oxygen evolution over $BiVO_4$ with AQE of 34.6%. *Nano Energy* **2021**, 81, 105651.

(29) Yang, Q.; Li, Y.; Xia, Z.; Chang, W.; Xing, Y. Preparation of two-dimensional mesoporous Ta_3N_5 by utilizing a biological template for enhanced photocatalytic hydrogen production. *Ceram. Int.* Doi: 10.1016/j.ceramint.2022.04.234.

(30) Li, S.; Cai, M.; Wang, C.; Liu, Y.; Li, N.; Zhang, P.; Li, X. Rationally designed Ta_3N_5/BiOCl S-scheme heterojunction with oxygen vacancies for elimination of tetracycline antibiotic and Cr (VI): performance, toxicity evaluation and mechanism insight. *J. Mater. Sci. Technol.* **2022**, 123, 177-190.

(31) He, R.; Ou, S.; Liu, Y.; Liu, Y.; Xu, D. In situ fabrication of Bi_2Se_3/g-C_3N_4 S-scheme photocatalyst with improved photocatalytic activity. *Chin. J. Catal.* **2022**, 43, 370-378.

(32) Zhou, L.; Li, Y.; Zhang, Y.; Qiu, L.; Xing, Y. A 0D/2D $Bi_4V_2O_{11}$/g-C_3N_4 S-scheme heterojunction with rapid interfacial charges migration for photocatalytic antibiotic degradation. *Acta Phys. -Chim. Sin.* **2022**, 38, 2112027.

(33) Li, Y.; Li, X.; Zhang, H.; Fan, J.; Xiang, Q. Design and application of active sites in g-C_3N_4-based photocatalysts. *J. Mater. Sci. Technol.* **2020**, 56, 69-88.

(34) Li, Y.; Zhang, M.; Zhou, L.; Yang, S.; Wu, Z.; Ma, Y. Recent advances in surface-modified g-C_3N_4-based photocatalysts for H_2 production and CO_2 reduction. *Acta Phys. -Chim. Sin.* **2021**, 37, 2009030.

(35) Bi, S.; Yang, C.; Zhang, W.; Xu, J.; Liu, L.; Wu, D.; Wang, X.; Han, Y.; Liang, Q.; Zhang, F. Two-dimensional semiconducting covalent organic frameworks via condensation at arylmethyl carbon atoms. *Nat. Commun.* **2019**, 10, 2467.

(36) Che, H.; Li, C.; Li, C.; Liu, C.; Dong, H.; Song, X. Benzoyl isothiocyanate as a precursor to design of ultrathin and high-crystalline g-C_3N_4-based donor-acceptor conjugated copolymers for superior photocatalytic H_2 production. *Chem. Eng. J.* **2021**, 410, 127791.

(37) Fei, X.; Tan, H.; Cheng, B.; Zhu, C.; Zhang, L. 2D/2D black phosphorus g-C_3N_4 S-scheme heterojunction photocatalysts for CO_2 reduction investigated using DFT calculations. *Acta Phys. -Chim. Sin.* **2021**, 37, 2010027.

(38) Li, Y.; Zhou, M.; Cheng, B.; Shao, Y. Recent advances in g-C_3N_4-based heterojunction photocatalysts. *J. Mater. Sci. Technol.* **2020**, 56, 1-17.

(39) Li, Y.; Xia, Z.; Yang, Q.; Wang, L.; Xing, Y. Review on g-C_3N_4-based S-scheme heterojunction photocatalyst. *J. Mater. Sci. Technol.* **2022**, 125, 128-144.

(40) Liu, C.; Dai, H.; Tan, C.; Pan, Q.; Hu, F.; Peng, X. Photo-Fenton degradation of tetracycline over Z-scheme Fe-g-C_3N_4/Bi_2WO_6 heterojunctions: mechanism insight, degradation pathways and DFT calculation. *Appl. Catal. B* **2022**, 310, 121326.

(41) Liu, M.; He, N.; Guo, H.; Ying, S.; Chen, Z. Microwave pyrolysis and electrochemical supercapacitor of S-doped g-C_3N_4 nanoparticles. *Chin. J. Struct. Chem.* **2021**, 40, 806-810.

(42) Nasir, M.; Yang, G.; Ayub, I.; Wang, S.; Wang, L.; Wang, X.; Yan, W.; Peng, S.; Ramakarishna, S. Recent development in graphitic carbon nitride based photocatalysis for hydrogen generation. *Appl. Catal. B* **2019**, 257, 117855.

(43) Wang, Y.; Shen, S. Progress and prospects of non-metal doped graphitic carbon nitride for improved photocatalytic performances. *Acta Phys. -Chim. Sin.* **2020**, 36, 1905080.

(44) Liu, L.; Chen, F.; Wu, J.; Ke, M.; Cui, C.; Chen, J. Edge electronic vacancy on ultrathin carbon nitride nanosheets anchoring O_2 to boost H_2O_2 photoproduction. *Appl. Catal. B* **2022**, 302, 120845.

(45) Yuan, A.; Lei, H.; Xi, F.; Liu, J.; Qin, L.; Chen, Z.; Dong, X. Graphene quantum dots decorated graphitic carbon nitride nanorods for photocatalytic removal of antibiotics. *J. Colloid Interface Sci.* **2019**, 548, 56-65.

(46) Han, Q.; Wang, B.; Zhao, Y.; Hu, C.; Qu, L. A graphitic-C_3N_4 "Seaweed" architecture for enhanced hydrogen evolution. *Angew. Chem. Int. Ed.* **2015**, 54, 11433-11437.

(47) Zhang, L.; Zhang, J.; Yu, H.; Yu, J. Emerging S-scheme photocatalyst. *Adv. Mater.* **2022**, 34, 2107668.

(48) Zhu, B.; Cheng, B.; Fan, J.; Ho, W.; Yu, J. g-C_3N_4-based 2D/2D composite heterojunction photocatalyst. *Small Struct.* **2021**, 2, 2100086.

DOI: 10.14102/j.cnki.0254-5861.2022-0152

(49) Jiang, J.; Xiong, Z.; Wang, H.; Liao, G.; Bai, S.; Zou, J.; Wu, P.; Zhang, P.; Li, X. Sulfur-doped g-C_3N_4/g-C_3N_4 isotype step-scheme heterojunction for photocatalytic H_2 evolution. *J. Mater. Sci. Technol.* **2022**, 118, 15-24.
(50) He, F.; Wang, Z.; Li, Y.; Peng, S.; Liu, B. The nonmetal modulation of composition and morphology of g-C_3N_4-based photocatalysts. *Appl. Catal. B* **2020**, 269, 118828.
(51) Lv, H.; Huang, Y.; Koodali, R.; Liu, G.; Zeng, Y.; Meng, Q.; Yuan, M. Synthesis of sulfur-doped 2D graphitic carbon nitride nanosheets for efficient photocatalytic degradation of phenol and hydrogen evolution. *ACS Appl. Mater. Inter.* **2020**, 12, 12656-12667.
(52) Kumar, A.; Yadav, R.; Park, N.; Baeg, J. Facile one-pot two-step synthesis of novel in situ selenium-doped carbon nitride nanosheet photocatalysts for highly enhanced solar fuel production from CO_2. *ACS Appl. Nano Mater.* **2018**, 1, 47-54.
(53) Chu, Y.; Lin, T.; Lin, Y.; Chiu, W.; Nguyen, B.; Hu, C. Influence of P,S,O-doping on g-C_3N_4 for hydrogel formation and photocatalysis: an experimental and theoretical study. *Carbon* **2020**, 169, 338-348.
(54) Chuaicham, C.; Karthikeyan, S.; Pawar, R.; Xiong, Y.; Dabo, I.; Ohtani, B.; Kim, Y.; Song, J.; Ishihara, T.; Sasaki, K. Energy-resolved distribution of electron traps for O/S-doped carbon nitrides by reversed double-beam photoacoustic spectroscopy and the photocatalytic reduction of Cr (VI). *Chem. Commun.* **2020**, 56, 3793-3796.
(55) Yang, C.; Teng, W.; Song, Y.; Cui, Y. C-I codoped porous g-C_3N_4 for superior photocatalytic hydrogen evolution. *Chin. J. Catal.* **2018**, 39, 1615-1624.
(56) Liu, Q.; Shen, J.; Yu, X.; Yang, X.; Liu, W.; Yang, J.; Tang, H.; Xu, H.; Li, H.; Li, Y.; Xu, J. Unveiling the origin of boosted photocatalytic hydrogen evolution in simultaneously (S, P, O)-codoped and exfoliated ultrathin g-C_3N_4 nanosheets. *Appl. Catal. B* **2019**, 248, 84-94.
(57) Tian, Y.; Tian, X.; Zeng, W.; Nie, Y.; Yang, C.; Dai, C.; Li, Y.; Lu, L. Enhanced peroxymonosulfate decomposition into $^{\bullet}OH$ and $^1O_2$ for sulfamethoxazole degradation over Se doped g-C_3N_4 due to induced exfoliation and N vacancies formation. *Sep. Purif. Technol.* **2021**, 267, 118664.
(58) Huang, X.; Song, J.; Hua, M.; Chen, B.; Xie, Z.; Liu, H.; Zhang, Z.; Meng, Q.; Han, B. Robust selenium-doped carbon nitride nanotubes for selective electrocatalytic oxidation of furan compounds to maleic acid. *Chem. Sci.* **2021**, 12, 6342-6349.
(59) An, S.; Zhang, G.; Li, K.; Huang, Z.; Wang, X.; Guo, Y.; Hou, J.; Song, C.; Guo, X. Self-supporting 3D carbon nitride with tunable n→π* electronic transition for enhanced solar hydrogen production. *Adv. Mater.* **2021**, 33, 2104361.
(60) Gao, B.; Wang, J.; Dou, M.; Huang, X.; Yu, X. Novel nitrogen-rich g-C_3N_4 with adjustable energy band by introducing triazole ring for cefotaxime removal. *Sep. Purif. Technol.* **2020**, 241, 116576.
(61) Zhang, J.; Liao, H.; Sun, S. Construction of 1D/1D WO_3 nanorod/TiO_2 nanobelt hybrid heterostructure for photocatalytic application. *Chin. J. Struct. Chem.* **2020**, 39, 1019-1028.
(62) Liao, Y.; Yang, J.; Wang, G.; Wang, J.; Wang, K.; Yan, S. Hierarchical porous NiO as a noble-metal-free cocatalyst for enhanced photocatalytic H_2 production of nitrogen-deficient g-C_3N_4. *Rare Met.* **2022**, 41, 396-405.
(63) Liang, Z.; Shen, R.; Ng, Y.; Zhang, P.; Xiang, Q.; Li, X. A review on 2D MoS_2 cocatalysts in photocatalytic H_2 production. *J. Mater. Sci. Technol.* **2020**, 56, 89-121.
(64) Li, G.; Wang, B.; Wang, R. g-C_3N_4/Ag/GO composite photocatalyst with efficient photocatalytic performance: synthesis, characterization, kinetic studies, toxicity assessment and degradation mechanism. *Chin. J. Struct. Chem.* **2020**, 39, 1675-1688.
(65) Li, X.; Liu, J.; Huang, J.; He, C.; Feng, Z.; Chen, Z.; Wang, L.; Deng, F. All organic S-scheme heterojunction PDI-Ala/S-C_3N_4 photocatalyst with enhanced photocatalytic performance. *Acta Phys. -Chim. Sin.* **2021**, 37, 2010030.
(66) Liu, B.; Bie, C.; Zhang, Y.; Wang, L.; Li, Y.; Yu, J. Hierarchically porous ZnO/g-C_3N_4 S-scheme heterojunction photocatalyst for efficient H_2O_2 production. *Langmuir* **2021**, 37, 14114-14124.

Received: June 9, 2022
Accepted: June 18, 2022
Published: June 20, 2022

DOI: 10.14102/j.cnki.0254-5861.2022-0152